Effects of Low Reynolds Number on Wake-Generated Unsteady Flow of an Axial-Flow Turbine Rotor

Takayuki Matsunuma

National Institute of Advanced Industrial Science and Technology (AIST), 1-2-1 Namiki, Tsukuba, Ibaraki 305-8564, Japan
Email: t-matsunuma@aist.go.jp

Yasukata Tsutsui

National Institute of Advanced Industrial Science and Technology (AIST), 1-2-1 Namiki, Tsukuba, Ibaraki 305-8564, Japan
Email: y.tsutsui@aist.go.jp

The unsteady flow field downstream of axial-flow turbine rotors at low Reynolds numbers was investigated experimentally using hot-wire probes. Reynolds number, based on rotor exit velocity and rotor chord length $Re_{out,RT}$, was varied from 3.2×10^4 to 12.8×10^4 at intervals of 1.6×10^4 by changing the flow velocity of the wind tunnel. The time-averaged and time-dependent distributions of velocity and turbulence intensity were analyzed to determine the effect of Reynolds number. The reduction of Reynolds number had a marked influence on the turbine flow field. The regions of high turbulence intensity due to the wake and the secondary vortices were increased dramatically with the decreasing Reynolds number. The periodic fluctuation of the flow due to rotor-stator interaction also increased with the decreasing Reynolds number. The energy-dissipation thickness of the rotor midspan wake at the low Reynolds number $Re_{out,RT} = 3.2 \times 10^4$ was 1.5 times larger than that at the high Reynolds number $Re_{out,RT} = 12.8 \times 10^4$. The curve of the -0.2 power of the Reynolds number agreed with the measured energy-dissipation thickness at higher Reynolds numbers. However, the curve of the -0.4 power law fitted more closely than the curve of the -0.2 power law at lower Reynolds numbers below 6.4×10^4.

Keywords and phrases: axial-flow turbine, unsteady flow, rotor-stator interaction, low Reynolds number, wake, energy-dissipation thickness.

1. INTRODUCTION

With the new generation of small gas-turbine engines, low Reynolds number flows have become increasingly important. Blade Reynolds numbers for the turbine stage of such gas turbines can drop to below 10^5. For example, the Reynolds numbers of the turbine cascades of 300 kW industrial ceramic gas turbines (Arakawa et al. [1]) are approximately 6×10^4 because of the increased viscosity caused by high turbine-inlet temperatures and the miniaturization of the cascade, considerably smaller than the Reynolds numbers of conventional gas turbines. At these low Reynolds numbers, the boundary layer is dominated by laminar flow and is susceptible to flow separation and strong secondary vortices that develop into increased loss, leading to reduced performance. Small gas turbines for aircraft propulsion also encounter the low Reynolds number problem at high altitudes where the air

density is low. Several studies focusing on the aerodynamics of turbine cascades at low Reynolds numbers have recently been published. In experiments on linear cascades by Curtis et al. [2], Murawski et al. [3], Schulte and Hodson [4], Howell et al. [5], and Van Treuren et al. [6], flow separation occurred at the blade suction surface and the profile loss rapidly increased when the Reynolds number was reduced. Bons et al. [7] attempted to reduce the separation region on the suction surface at low Reynolds numbers using a method of intermittently blowing jets out from the blade surface. However, many unknown issues remain. In addition, these studies were limited to linear two-dimensional cascades. There have been few studies on annular three-dimensional cascades at low Reynolds numbers.

Moreover, the flow field around the blades of a turbine is very unsteady and complex due to rotor-stator interaction, the aerodynamic interaction between the turbine nozzle (stator) and the turbine rotor. Boundary layer behavior, loss generation, secondary-vortex growth, and heat transfer in turbines are strongly affected by the rotor-stator interaction. Even though unsteady flow plays an important role
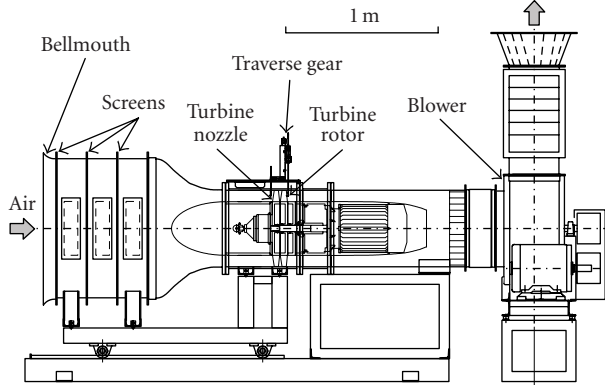
FIGURE 1: Annular turbine wind tunnel.

FIGURE 2: Geometry of turbine nozzle: (a) tip, (b) midspan, and (c) hub.

FIGURE 3: Geometry of turbine rotor: (a) tip, (b) midspan, and (c) hub.

in axial-flow turbines, turbines are designed using steady-flow calculations. Because no actual models exist for the loss-generating mechanisms seen in an unsteady flow, empirical correlations are used to account for the effects of unsteadiness. More knowledge on unsteady rotor-stator interaction is essential to increase the performance of turbines (Sharma et al. [8], Kost et al. [9]) especially at low Reynolds numbers. Although a variety of measurement techniques can be easily applied to the flow field within the stationary blades, difficulties arise with the measurements of the flow field within the rotating blades. Direct measurements of turbine rotor flows using rotating devices have been conducted by Hodson [10] and Chaluvadi et al. [11]. Binder et al. [12], Zaccaria and Lakshminarayana [13, 14], and Matsunuma and Tsutsui [15] used laser measurement systems, such as laser two-focus velocimetry (L2F) and laser Doppler velocimetry (LDV). Sharma et al. [8], Binder et al. [16], and Gallus et al. [17] used hot-wire probes in a stationary frame downstream of the rotor. Since there have been few reports on unsteady rotor flow at low Reynolds numbers, and no reliable computational analyses are available to compute low Reynolds number turbine flows (Halstead et al. [18]), detailed experimental data will make a major important contribution to establishing theoretical studies.

2. EXPERIMENTAL FACILITY AND METHOD

2.1. Annular wind tunnel and turbine cascades

Figure 1 shows the annular turbine wind tunnel used in our experiments. This wind tunnel is an air-suction type with open circuit facility. The total length of the wind tunnel is approximately 3.8 meters. The outer and inner annular wall diameters of the test section are 500 mm and 350 mm, respectively. A single-stage axial-flow turbine designed using a free vortex method to attain radial equilibrium was installed at the test section. An incremental rotary encoder (1 800 pulses/revolution) was attached to the rotor shaft to detect the rotor's angular position. The geometries and specifications of the nozzle and rotor cascades are shown in Figures 2 and 3 and in Table 1.
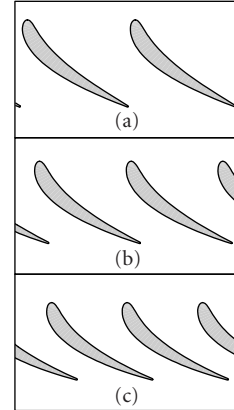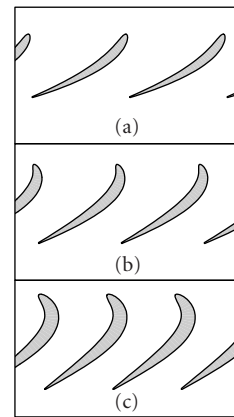
TABLE 1: Specifications of turbine cascades.

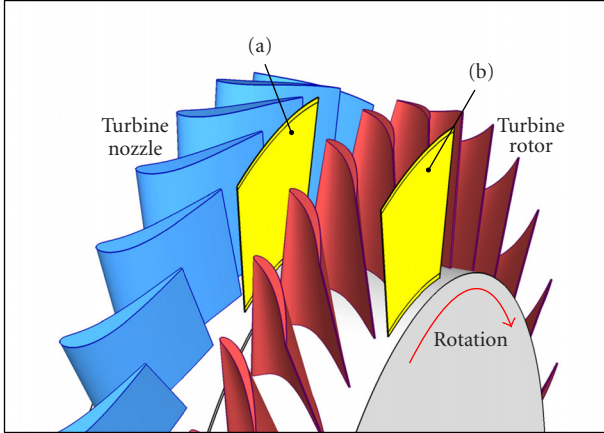|	Nozzle			Rotor		
	Tip	Mid	Hub	Tip	Mid	Hub
Number of blades, N	—	28	—	—	31	—
Chord, C (mm)	69.1	67.6	66.1	58.5	58.5	58.5
Axial chord, C_{ax} (mm)	45.0	42.5	40.0	32.3	40.9	48.0
Blade span, H (mm)	—	75.0	—	—	74.0	—
Blade pitch, S (mm)	56.1	47.7	39.3	50.7	43.1	35.5
Aspect ratio, H/C	1.09	1.10	1.13	1.26	1.26	1.26
Solidity, C/S	1.23	1.42	1.68	1.15	1.42	1.65
Inlet flow angle, α_1 (deg)	0.0	0.0	0.0	−16.5	21.8	51.7
Exit flow angle, α_2 (deg)	63.9	67.4	71.1	66.9	63.4	58.7
Stagger angle, ξ (deg)	49.3	51.0	52.7	55.9	47.6	33.4
Inner diameter, D_1 (mm)	—	350	—	—	350	—
Outer diameter, D_2 (mm)	—	500	—	—	500	—
Hub/tip ratio, D_1/D_2	—	0.7	—	—	0.7	—
Tip clearance, τ (mm)	—	0.0	—	—	1.0	—

FIGURE 4: Measurement locations. (a) Measuring plane at nozzle exit ($Z_{NZ}/C_{ax,NZ} = 1.156$, $Z_{RT}/C_{ax,RT} = -0.517$). (b) Measuring plane at rotor exit ($Z_{RT}/C_{ax,RT} = 1.252$).

FIGURE 5: Measuring plane at the nozzle exit. (a) $Z_{NZ}/C_{ax,NZ} = 1.156$, $Z_{RT}/C_{ax,RT} = -0.517$.

2.2. Experimental instruments and methods

Figure 4 shows the measurement locations of the turbine nozzle and rotor.

Measurements of nozzle exit flow (rotor inlet flow)

The wake traverse of the nozzle was carried out at a distance 6.6 mm axially from the nozzle trailing edge, that is, $Z_{NZ}/C_{ax,NZ} = 1.156$ (at a -21.2 mm axial distance from the rotor leading edge, that is, $Z_{RT}/C_{ax,RT} = -0.517$). The distributions of total pressure, velocity, flow angle and so forth were obtained using a 5-hole pressure probe with a head diameter of 2.1 mm. The distributions of turbulence intensity were obtained using single-element hot-wire anemometry with 5 μm-diameter tungsten wire and active sensor length of 1 mm with (Model 0247R-T5, Kanomax Japan Inc.). Measurement accuracy of normalized velocity V/V_1 was estimated to be 0.0092 (0.92% of the reference velocity). The total number of measurement points in the yellow measuring plane at the nozzle exit in Figure 4 was 819 (21 spanwise $\times$ 39 pitchwise locations). The traverse mechanisms had resolutions of 0.004 mm in the spanwise direction and 0.0036 deg. in the pitchwise direction.

Measurements of rotor exit flow

The wake traverse of the rotor was carried out at an axial distance of 10.3 mm from the rotor trailing edge, that is, $Z_{RT}/C_{ax,RT} = 1.252$. The total number of measurement points in the yellow measuring plane at the rotor exit in Figure 4 was 1 365 (21 spanwise $\times$ 65 pitchwise locations). The time-dependent unsteady distributions of velocity and turbulence intensity were obtained using single-element hot-wire anemometry with 5μm-diameter tungsten wire and active sensor length 1 mm (Model 0248R-T5, Kanomax Japan Inc.). The hot-wire data synchronized with the rotary encoder pulses was recorded using a high-speed A/D converter (Model DL708E, Yokogawa Electric Corp.). Phase-locked
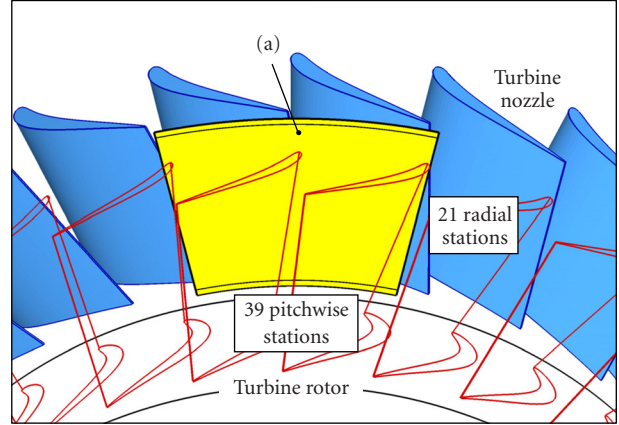
ensemble-average technique (Binder et al. [16]) was used to analyze the unsteady flow caused by the rotor-stator interaction. An automatic measurement system controlled by a desktop computer was adopted in this study, and all measured data was stored on the computer's hard disk.

2.3. Experimental conditions

The Reynolds number, based on nozzle inlet velocity and nozzle chord length $Re_{in,NZ}$, was varied from 1.7×10^4 to 6.6×10^4 at intervals of 0.8×10^4. Although the Reynolds numbers of a turbine cascade are generally based on exit flow conditions, during the experiments, the authors used the Reynolds numbers as parameters based on the nozzle inlet condition. This is because it was difficult to adjust the Reynolds number based on the rotor exit condition precisely during the experiments, especially under conditions of low Reynolds number with large separation and secondary-flow regions. The Reynolds numbers based on rotor exit mean velocity $Re_{out,RT}$ ranged from 3.2×10^4 to 12.8×10^4 as shown in Table 2. The rotor speed was varied from 402 rpm to 1 408 rpm to attain the same rotor inlet flow angle at various Reynolds numbers. The flow in this experiment was regarded as being incompressible because the Mach number based on the rotor exit conditions was very low, $M_{out,RT} = 0.023 \sim 0.093$.

3. RESULTS AND DISCUSSION

3.1. Nozzle exit flow (rotor inlet flow)

Figure 5 shows the measuring plane at the nozzle exit.

Figures 6 and 7 compare the distributions of the three-dimensional flow at nozzle exit ($Z_{NZ}/C_{ax,NZ} = 1.156$) at the lowest Reynolds number in this study, $Re_{out,NZ} = 4.3 \times 10^4$ ($Re_{out,RT} = 3.2 \times 10^4$), and the highest Reynolds number, $Re_{out,NZ} = 17.2 \times 10^4$ ($Re_{out,RT} = 12.8 \times 10^4$).

As illustrated in Figures 6a and 7a, the total pressure loss at the nozzle trailing edge increases with decreasing Reynolds number, due to the increasing thickness of the boundary

TABLE 2: Correspondence of Reynolds numbers.

Reynolds number				Rotor disk speed (rpm)
$Re_{in,NZ}$ (Nozzle inlet)	$Re_{out,NZ}$ (Nozzle exit)	$Re_{in,RT}$ (Rotor inlet)	$Re_{out,RT}$ (Rotor exit)	
1.7×10^4	4.3×10^4	1.6×10^4	3.2×10^4	402
2.5×10^4	6.4×10^4	2.3×10^4	4.8×10^4	603
3.3×10^4	8.6×10^4	3.1×10^4	6.4×10^4	804
4.1×10^4	10.7×10^4	3.8×10^4	7.9×10^4	1005
5.0×10^4	13.0×10^4	4.7×10^4	9.7×10^4	1206
5.8×10^4	15.1×10^4	5.4×10^4	11.3×10^4	1307
6.6×10^4	17.2×10^4	6.2×10^4	12.8×10^4	1408
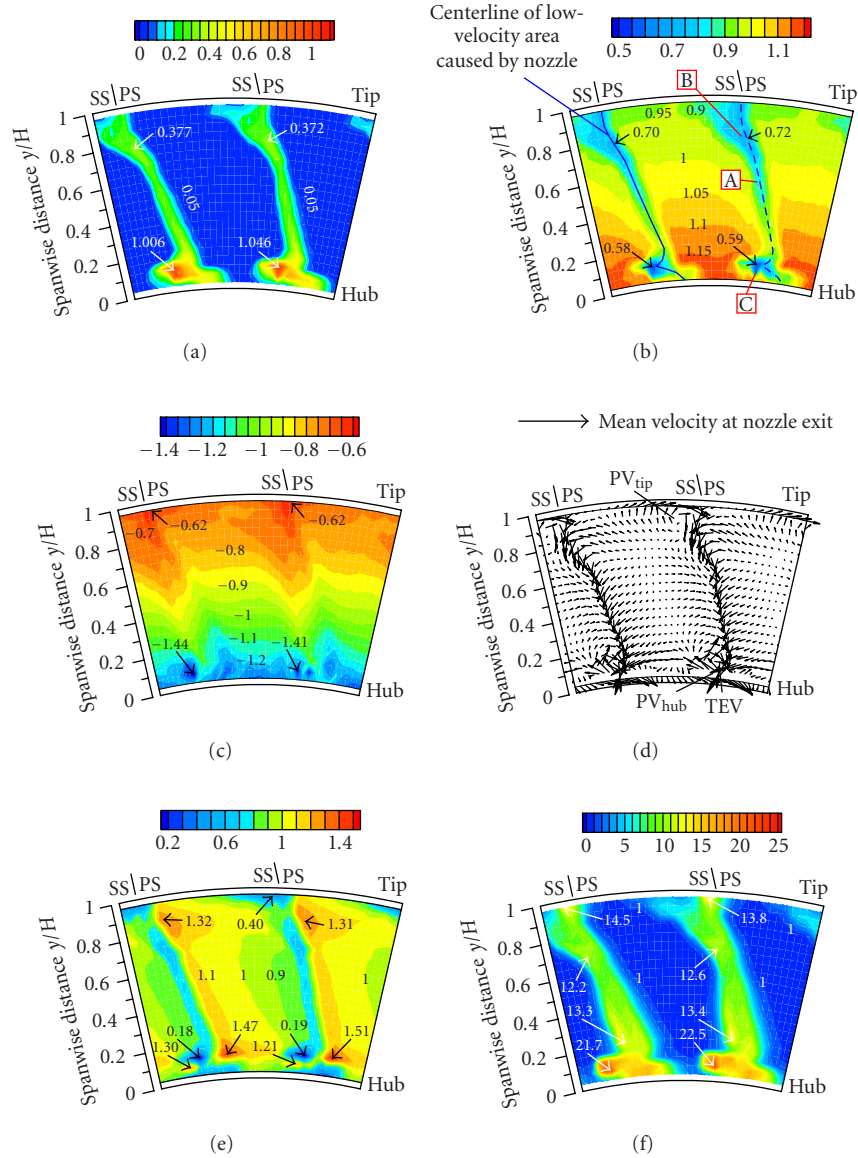
FIGURE 6: Distributions of the three-dimensional flow at nozzle exit (at rotor inlet). (Lowest Reynolds number $Re_{out,NZ} = 4.3 \times 10^4$, $Re_{out,RT} = 3.2 \times 10^4$.) (a) Total pressure loss CPt. (b) Absolute velocity V/V_1. (c) Static pressure CPs. (d) Secondary flow $\vec{Vs}$. (e) Axial velocity V_Z/V_{1Z}. (f) Turbulence intensity $Tu\%$.
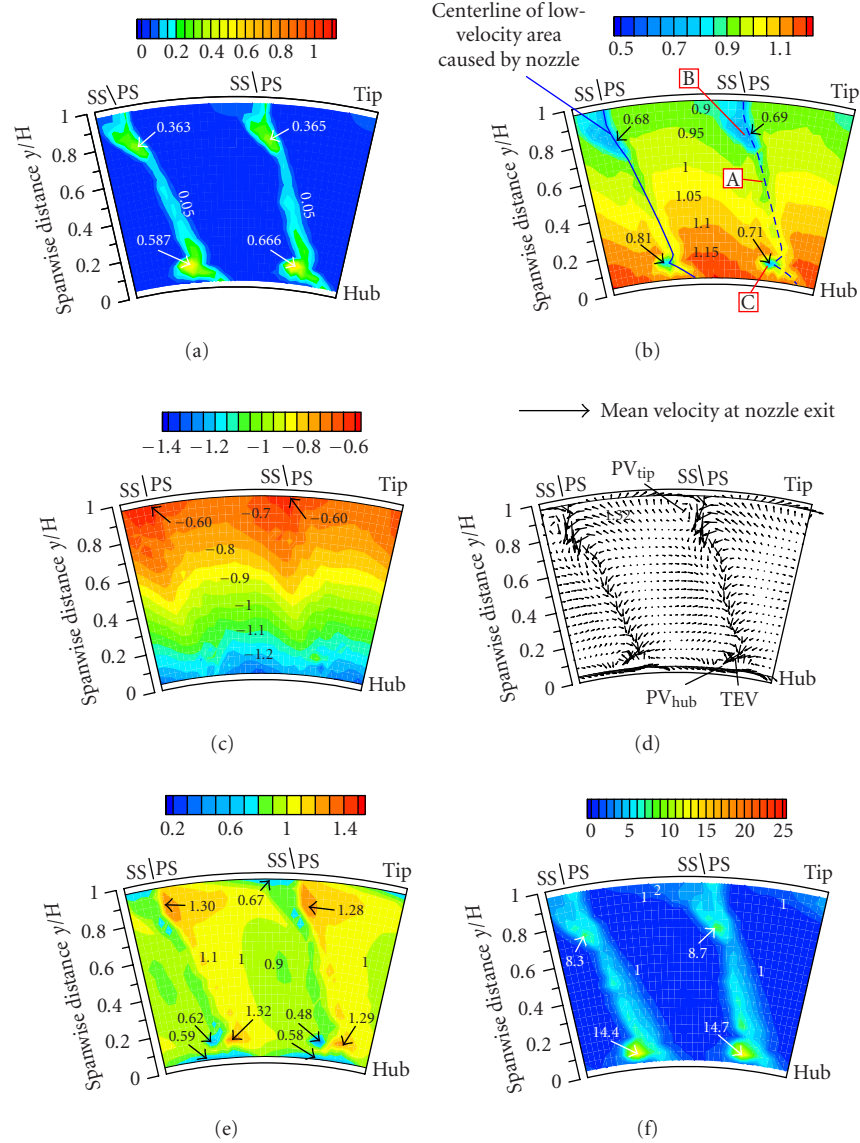
FIGURE 7: Distributions of the three-dimensional flow at nozzle exit (at rotor inlet). (Highest Reynolds number $Re_{out,NZ} = 17.2 \times 10^4$, $Re_{out,RT} = 12.8 \times 10^4$.) (a) Total pressure loss CPt. (b) Absolute velocity V/V_1. (c) Static pressure CPs. (d) Secondary flow $\overrightarrow{Vs}$. (e) Axial velocity V_Z/V_{1Z}. (f) Turbulence intensity Tu%.

layer on the nozzle surface, and due to the increase in the separation zone on the nozzle suction surface (SS). The regions of high total-pressure loss extend to near the tip and hub endwalls of the suction surface, since a passage vortex sweeps up the inlet-endwall boundary-layer fluid on the suction surface. The net overall loss generated in the nozzle passage at $Re_{out,NZ} = 4.3 \times 10^4$ (0.0771) was 1.64 times greater that at $Re_{out,NZ} = 17.2 \times 10^4$ (0.0471).

Figures 6b and 7b show the absolute velocity distributions. Decreasing the Reynolds number results in a deficit of the velocity behind the trailing edge (region A) and near the endwalls (regions B and C).

Figures 6d and 7d show a comparison of the distributions of secondary-flow vectors. Passage vortices (PV_{tip} and

PV_{hub}) are observed near the suction side of both tip and hub endwalls. The flow beside the trailing edge moves downward from the tip to the hub in the endwall direction due to the imbalance of the centrifugal force and the pressure gradient in the blade wake region. This strong inward wake at the trailing edge generates a clockwise vortex (TEV) near the hub endwall that collides with the counterclockwise hub passage vortex, PV_{hub}. The strong interaction between TEV and PV_{hub} generates a major high-loss region near the hub endwall. All secondary vortices, such as PV_{hub}, PV_{tip}, and TEV, grow with decreasing Reynolds number.

Figures 6f and 7f show the turbulence intensity distributions. The areas of high turbulence intensity conform to the areas of high loss in Figures 6a and 7a.
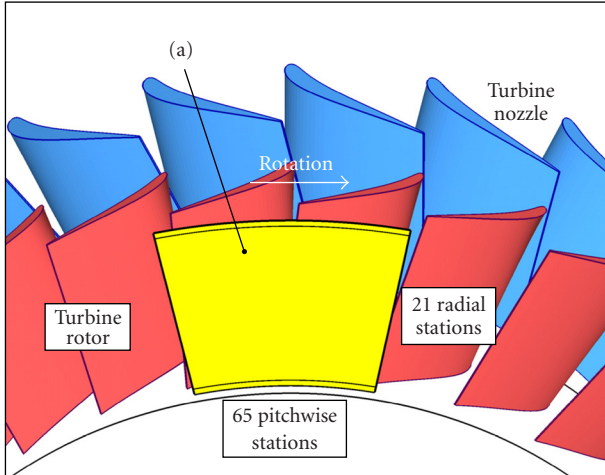
FIGURE 8: Measuring plane at the rotor exit. (a) $Z_{RT}/C_{ax,RT} = 1.252$.

3.2. Rotor exit flow

Figure 8 shows the measuring plane at the rotor exit. The rotor blades move from the left to the right in the figure.

Time-dependent unsteady flow

Figure 9 shows the time-dependent distributions of velocity and turbulence intensity at the rotor exit ($Z_{RT}/C_{ax,RT} = 1.252$) at $t = 1/29\,T_{RT}$ at the lowest Reynolds number $Re_{out,RT} = 3.2 \times 10^4$.

In Figure 9a, a large low-velocity region extends to near the hub endwall of the rotor suction surface (region D) because the turning angle of flow at the hub region is greater than that at the tip region, causing a strong passage to be generated. A low-velocity region is also present at the rotor suction side near the tip endwall (region E). These regions are generated by the interaction of the tip-side passage vortex and leakage vortex (tip clearance vortex). The velocity is low at the suction side of the rotor trailing edge (region F, the right region of the pink line) because of the flow separation on the rotor suction surface. The blue line in the figure indicates the centerline of the low-velocity area caused by the upstream nozzle effect. This blue line is considerably inclined compared with the nozzle wake just downstream of the nozzle in Figure 6b. The blue line is disconnected at the rotor trailing edge by the chop of the nozzle wake at the rotor leading edge, as shown later in Figure 10d.

Figure 9b shows the velocity defect obtained by subtracting the distribution of the time-averaged velocity in the rotating frame of reference in Figure 19 from the distribution of the time-dependent velocity in Figure 9a. The low-velocity region due to the nozzle wake effect can be clearly observed.

In Figure 9c, high turbulence intensity regions are present at the suction side near the hub ($y/H = 0.3$), at the suction side near the tip ($y/H = 0.9$), and at the mid-pitch near the tip, which correspond to the effects of the hub-side passage vortex PV_{hub}, the tip-side passage vortex PV_{tip}, and
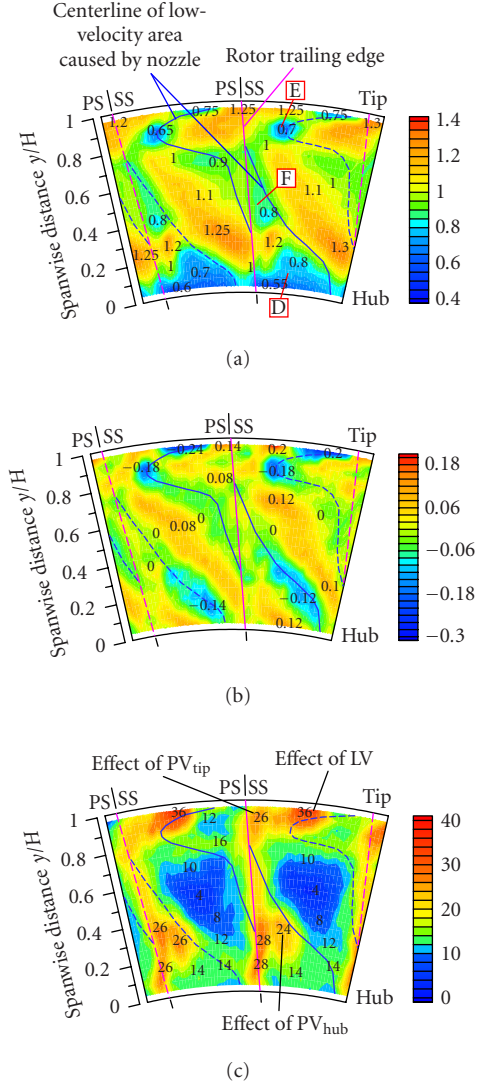

FIGURE 9: Time-dependent distributions at the rotor exit at $t = 1/29\,T_{RT}$. (Lowest Reynolds number $Re_{out,RT} = 3.2 \times 10^4$.) (a) Absolute velocity V/V_2. (b) Veolocity defect due to nozzle wake (velocity difference, Figure 9a–Figure 17a). (c) Turbulence intensity Tu%.

tip leakage vortex LV, respectively. High turbulence intensity regions are generated around the blue lines (the centerlines of the low-velocity regions due to the nozzle).

Figure 10 shows the time-dependent unsteady flow at midspan ($y/H = 0.5$), which was measured using a laser Doppler velocimetry (LDV) system (Matsunuma and Tsutsui [15]). The low-velocity area caused by the wake behind the nozzle affects the flow field around the rotor, as shown in Figures 10a and 10b. In the absolute coordinate system, the swirl flow that exits the nozzle decelerates in the rotor passage (Figures 10a and 10c). The high turbulence intensity region which corresponds to the wake can be clearly observed in Figure 10d. The straight lines of high turbulence intensity caused by the nozzle wake are chopped at the rotor leading
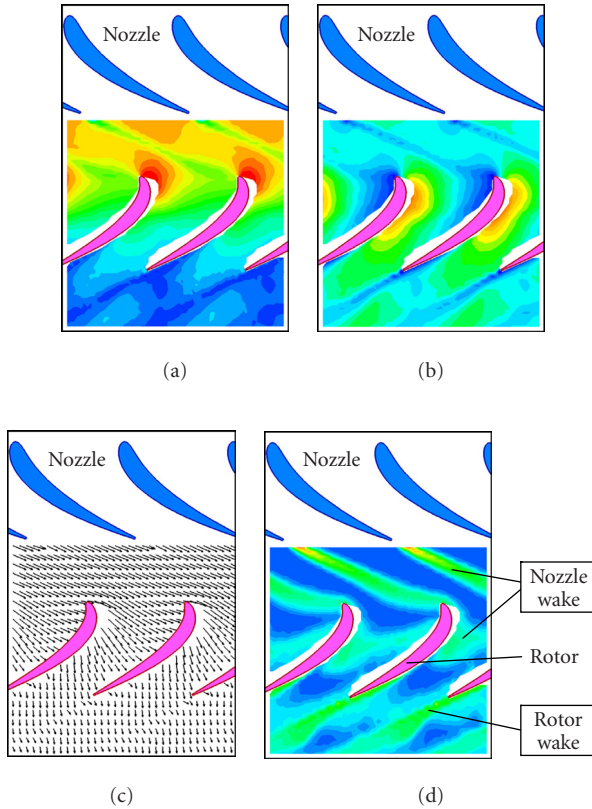
FIGURE 10: Time-dependent unsteady flow at midspan $y/H = 0.5$ (LDV measurements). (a) Absolute velocity. (b) Axial velocity. (c) Absolute velocity vector. (d) Turbulence intensity.

edge and distort when they pass through the rotor passage. The distortion of the nozzle wake in the rotor passage occurs because the flow region near the rotor suction surface moves faster than the flow near the rotor pressure surface. At the rotor exit, complex unsteady distributions of high turbulence intensity were formed by the merging of the nozzle and rotor wakes.

Figures 11 and 12 show a comparison of the velocity distributions at the rotor exit at the lowest Reynolds number $Re_{out,RT} = 3.2 \times 10^4$ and highest Reynolds number $Re_{out,RT} = 12.8 \times 10^4$. The time is divided into 29 time indices from $t = 1/29\, T_{RT}$ to $t = 29/29\, T_{RT}$, where T_{RT} indicates the time period of one-pitch movement of the rotor. The velocity distributions at eight time indices are shown in these figures. The velocity distributions fluctuate unsteadily because of rotor-stator interaction. The periodic fluctuation of the velocity due to the rotor-stator interaction increases with decreasing Reynolds number. These results highlight the importance of unsteady-flow analysis in the design of turbine blades operating at low Reynolds numbers.

Figures 13 and 14 show a comparison of the turbulence intensity distributions at the rotor exit at the lowest and highest Reynolds numbers. Turbulence intensity increases dramatically with decreasing Reynolds number.

Time-averaged flow

Figure 15 shows the time-averaged distributions at rotor exit in stationary (absolute) frame of reference. As a consequence of the time-averaging procedure from the stationary coordinate system which was fixed with the nozzle as shown in Figure 16, the rotor trailing edge is not visible in this figure. Each blue line indicates the centerline of the low-velocity area generated by the nozzle. The low-velocity area at the rotor exit is more slanted than that at the nozzle exit in Figures 6 and 7 because the nozzle exit flow angle at the hub is higher than that at the tip. Although the blue lines are straight from the hub endwall $y/H = 0.0$ to $y/H = 0.7$, they are skewed from $y/H = 0.7$ to the tip endwall $y/H = 1.0$. The skew near the tip is caused by the clockwise tip-side passage vortex of the nozzle, marked by PV_{tip} in Figures 6d and 7d. The velocity defects due to the nozzle effect increase with decreasing Reynolds number, as shown in Figures 15c and 15f.

Figure 17 shows the time-averaged distributions at the rotor exit in a rotating (relative) frame of reference. As a consequence of the time-averaging procedure from the rotating coordinate system which is moved with the rotor as shown in Figure 18, the nozzle effect is not visible in the figure. The velocity defects at the rotor suction side due to the wake and secondary vortices of the rotor increase with decreasing Reynolds number. The turbulence intensity also increases significantly with decreasing Reynolds number.

Figures 19 and 20 show the spanwise distributions of the time-averaged velocity and turbulence intensity at lower and higher Reynolds numbers. These distributions were obtained by calculating the pitchwise-averaged values of velocity and turbulence intensity over one rotor pitch in Figure 17. In Figure 19, the lowest velocity near the hub endwall decreases with decreasing Reynolds number because of the strengthened passage vortex. In Figure 20, the turbulence intensity increases rapidly with decreasing Reynolds number.

Figures 21 and 22 show the pitchwise distributions of time-averaged velocity and turbulence intensity at rotor midspan, $y/H = 0.5$, in rotating frame of reference. The velocity at the suction side of the rotor trailing edge was strongly affected by the Reynolds number. The turbulence intensity at the rotor suction side was extremely large. The maximum turbulence intensity at $Re_{out,RT} = 3.2 \times 10^4$ (0.065) was 1.5 times as large as that at $Re_{in} = 12.8 \times 10^4$ (0.045).

Figure 23 shows the energy-dissipation thickness of the wake at the rotor midspan in Figure 21. The energy-dissipation thickness, which corresponds to the loss, increases steadily with decreasing Reynolds number. The energy-dissipation thickness at the low Reynolds number $Re_{out,RT} = 3.2 \times 10^4$ (0.123) is 1.7 times greater than that at the high Reynolds number $Re_{out,RT} = 12.8 \times 10^4$ (0.073). At higher Reynolds numbers over 6.4×10^4, the measured data agrees with the curve of the -0.2 power of the Reynolds number, as shown in the blue line in the figure. This result conforms to the well-known fact that the losses in a turbine vary according to the -0.2 power of the Reynolds number
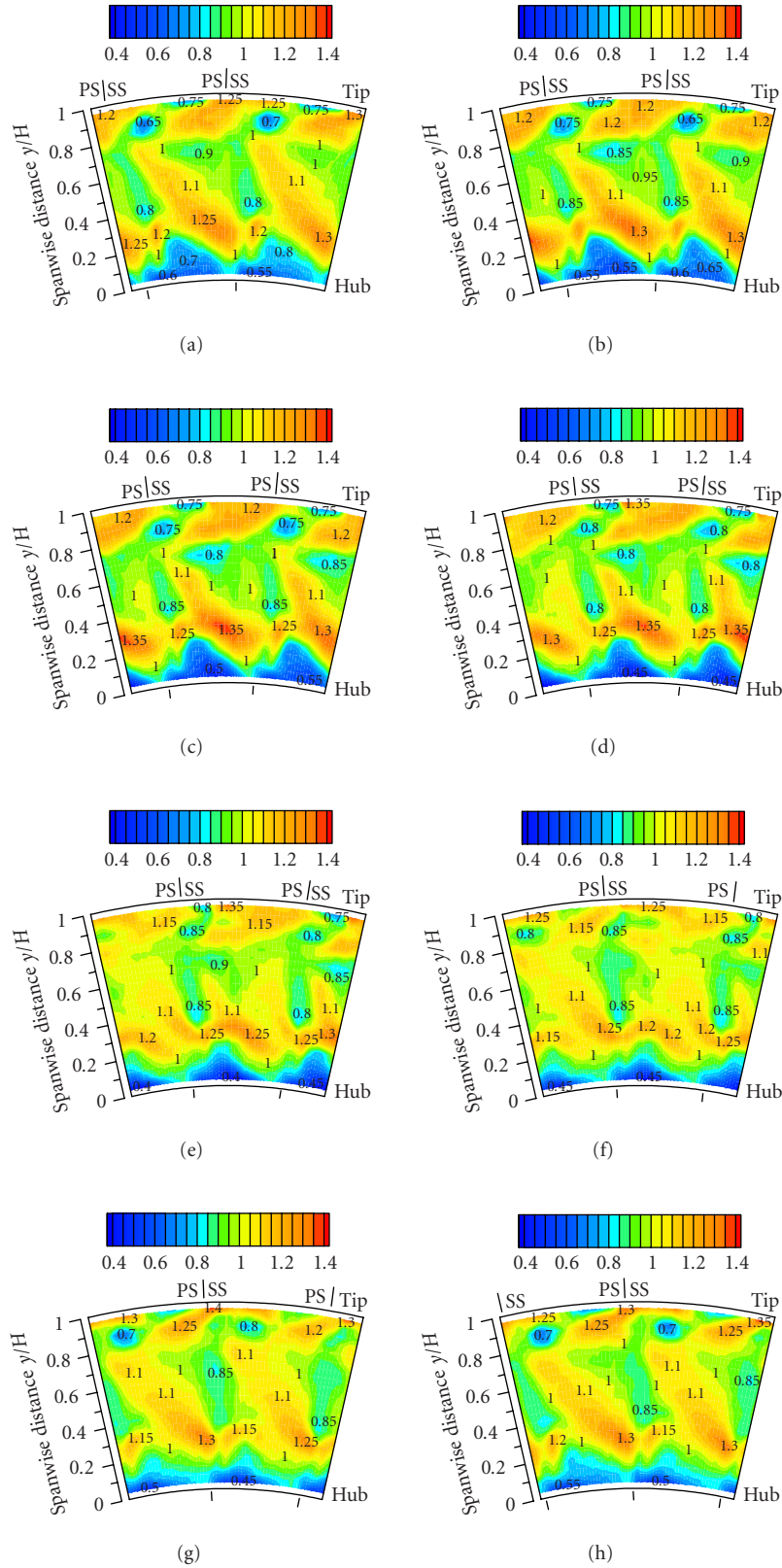
FIGURE 11: Time-dependent distributions of velocity V/V_2 at turbine rotor exit. (Lowest Reynolds number $Re_{out,RT} = 3.2 \times 10^4$.) (a) $t = 1/29T_{RT}$. (b) $t = 5/29T_{RT}$. (c) $t = 8/29T_{RT}$. (d) $t = 12/29T_{RT}$. (e) $t = 16/29T_{RT}$. (f) $t = 19/29T_{RT}$. (g) $t = 23/29T_{RT}$. (h) $t = 26/29T_{RT}$.
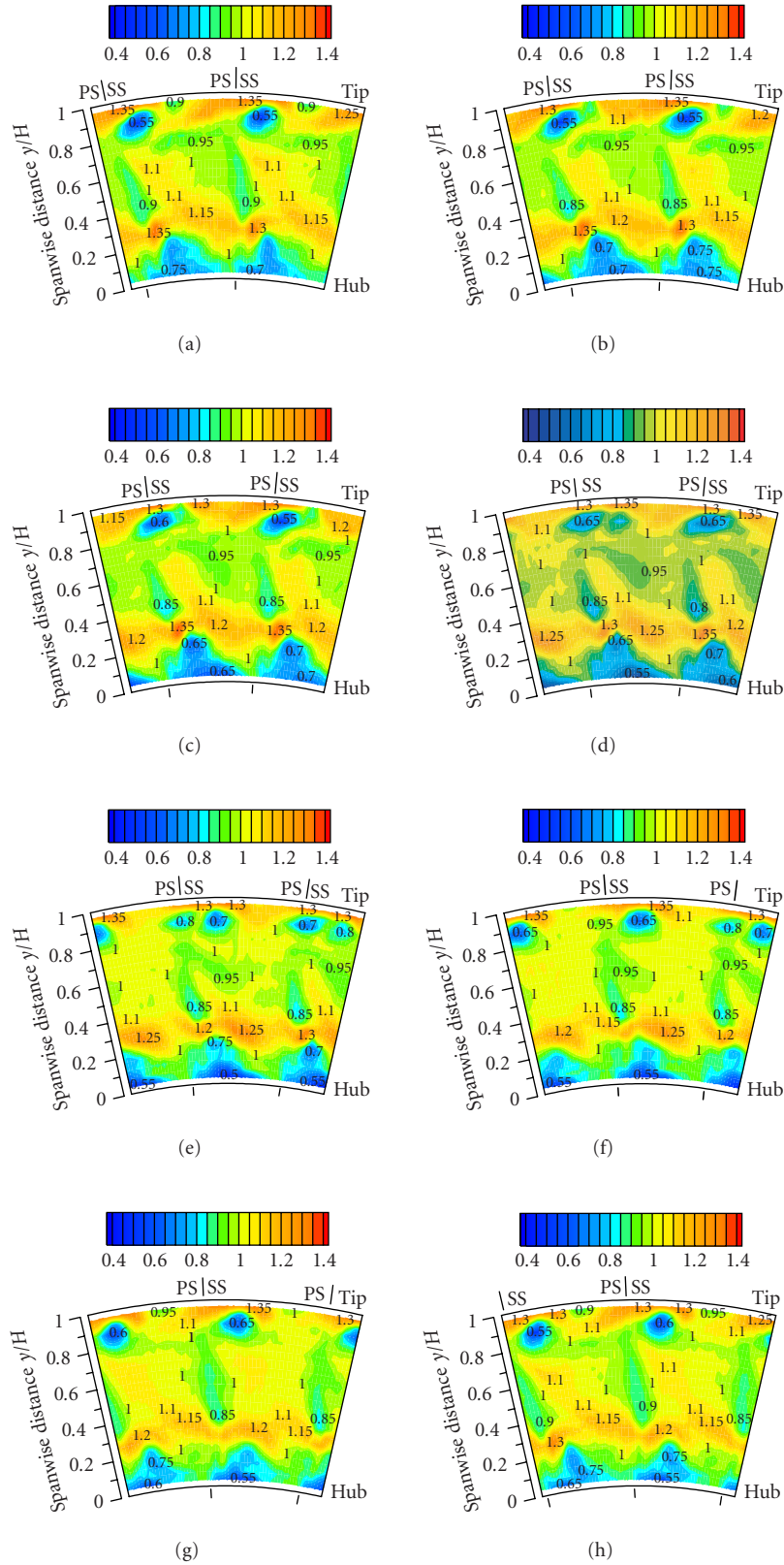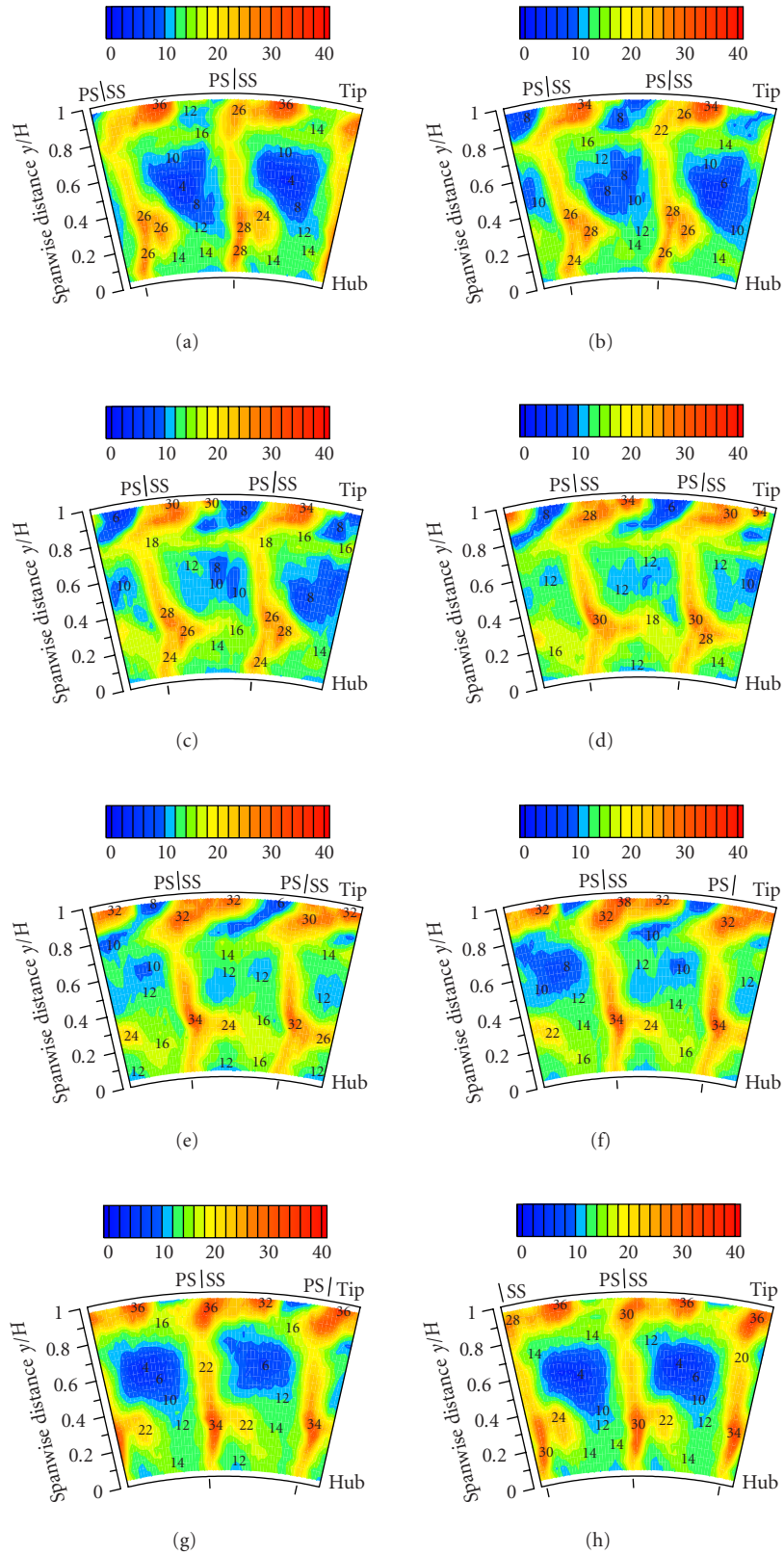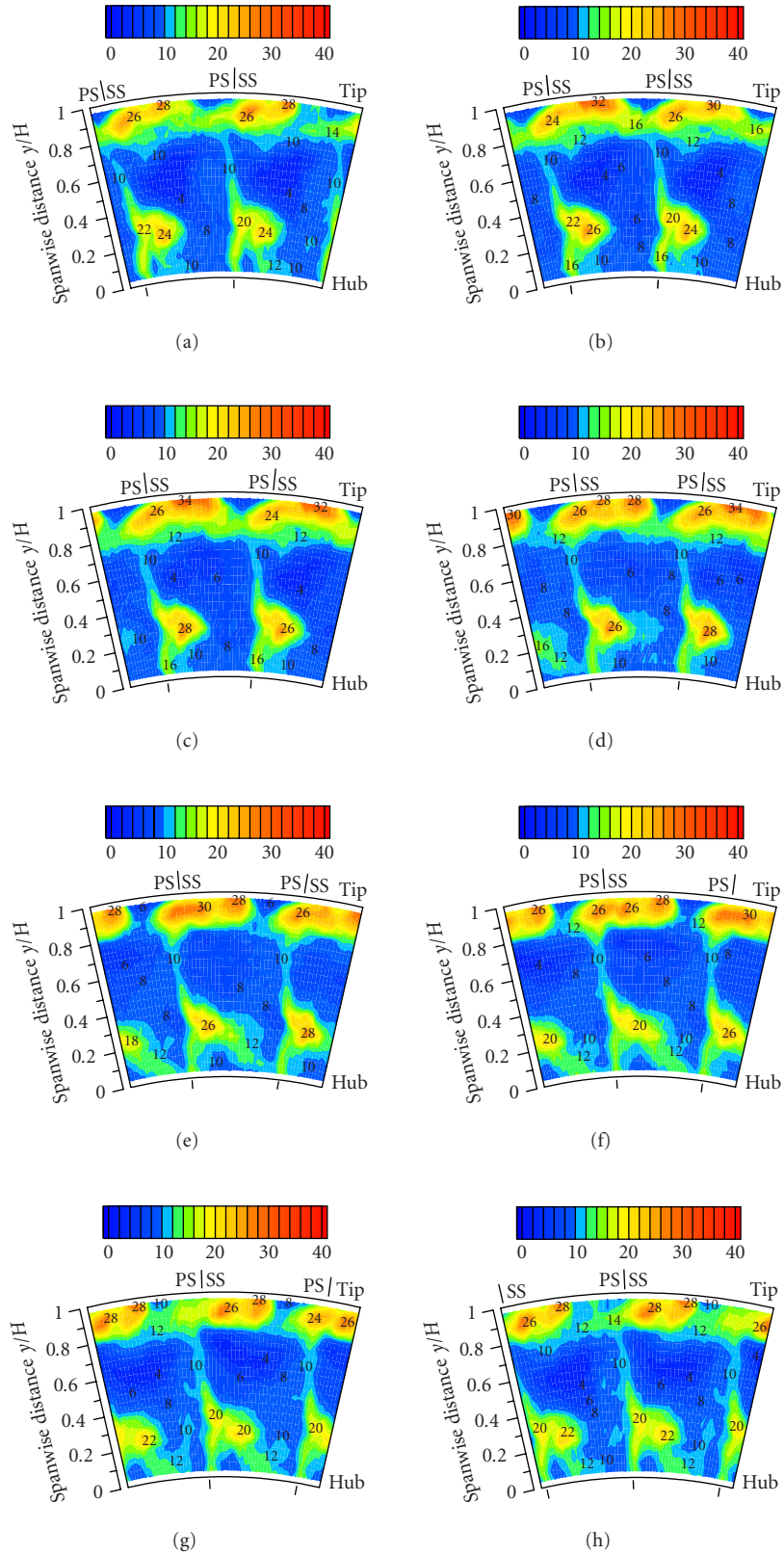
FIGURE 12: Time-dependent distributions of velocity V/V_2 at turbine rotor exit. (Highest Reynolds number $Re_{out,RT} = 12.8 \times 10^4$.) (a) $t = 1/29T_{RT}$. (b) $t = 5/29T_{RT}$. (c) $t = 8/29T_{RT}$. (d) $t = 12/29T_{RT}$. (e) $t = 16/29T_{RT}$. (f) $t = 19/29T_{RT}$. (g) $t = 23/29T_{RT}$. (h) $t = 26/29T_{RT}$.

FIGURE 13: Time-dependent distributions of turbulence intensity Tu % at turbine rotor exit. (Lowest Reynolds number $\mathrm{Re}_{\mathrm{out,RT}}$ = 3.2×10^4.) (a) $t = 1/29 T_{\mathrm{RT}}$. (b) $t = 5/29 T_{\mathrm{RT}}$. (c) $t = 8/29 T_{\mathrm{RT}}$. (d) $t = 12/29 T_{\mathrm{RT}}$. (e) $t = 16/29 T_{\mathrm{RT}}$. (f) $t = 19/29 T_{\mathrm{RT}}$. (g) $t = 23/29 T_{\mathrm{RT}}$. (h) $t = 26/29 T_{\mathrm{RT}}$.

FIGURE 14: Time-dependent distributions of turbulence intensity Tu % at turbine rotor exit. (Highest Reynolds number $Re_{out,RT} = 12.8 \times 10^4$.) (a) $t = 1/29T_{RT}$. (b) $t = 5/29T_{RT}$. (c) $t = 8/29T_{RT}$. (d) $t = 12/29T_{RT}$. (e) $t = 16/29T_{RT}$. (f) $t = 19/29T_{RT}$. (g) $t = 23/29T_{RT}$. (h) $t = 26/29T_{RT}$.

(a)

(b)

(c)

(d)

(e)

(f)
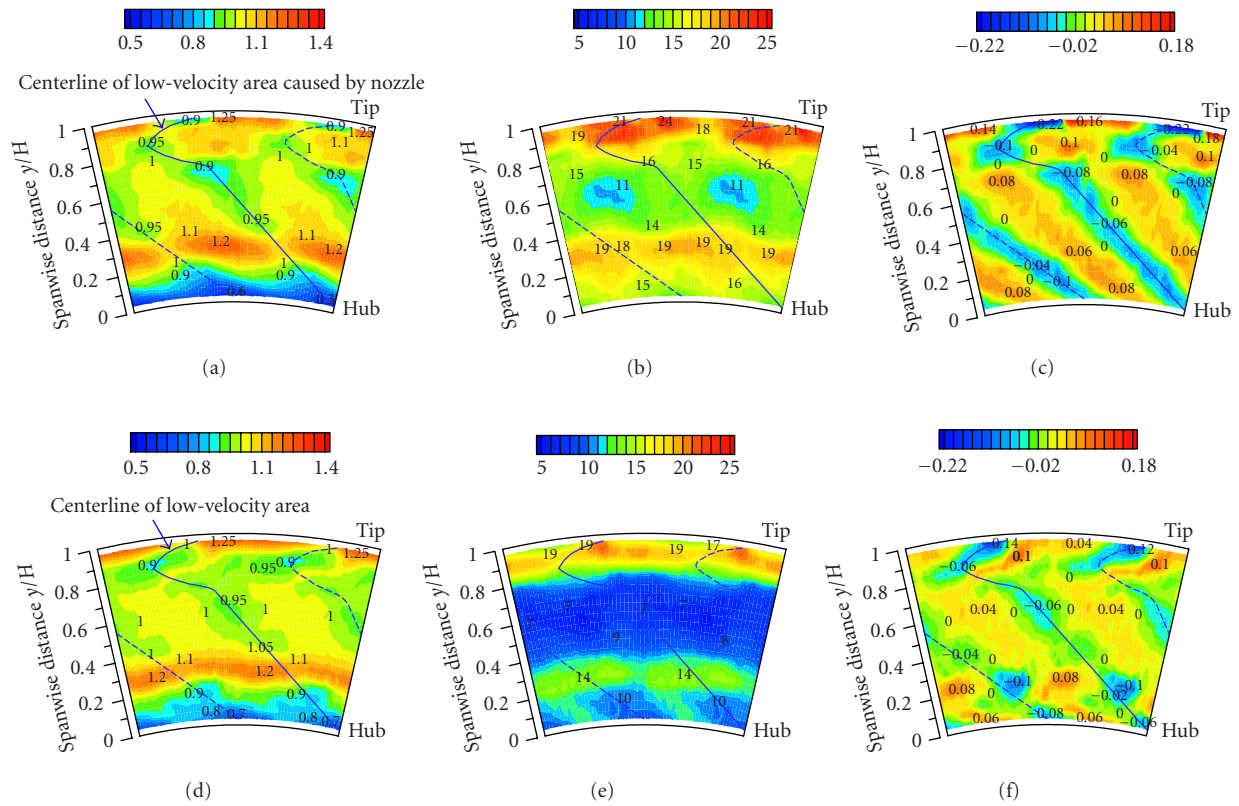
FIGURE 15: Time-averaged distributions at rotor exit in stationary frame of reference (nozzle effect). (a) and (d) Velocity V/V_2. (b) and (e) Turbulence intensity Tu%. (c) and (f) Velocity defect due to nozzle difference, **Figure 15a**–**Figure 19** ((a), (b), and (c) Lowest Reynolds number $Re_{out,RT} = 3.2 \times 10^4$. (d), (e), and (f) Highest Reynolds number $Re_{out,RT} = 12.8 \times 10^4$).
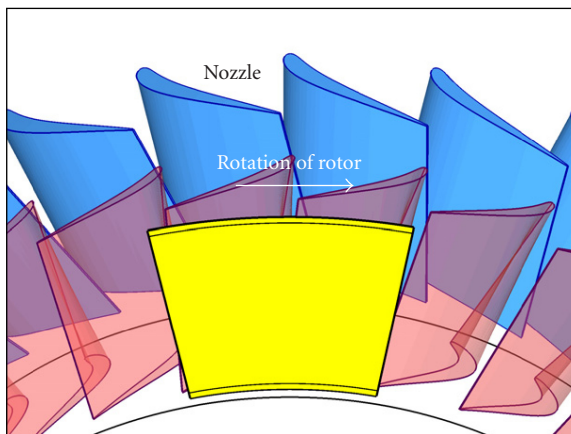
FIGURE 16: Stationary frame of reference in **Figure 15**.

(Fielding [19]). However, the curve of the -0.2 power law did not match up to the measured data at Reynolds numbers below 6.4×10^4. At lower Reynolds numbers, the curve of the -0.4 power of the Reynolds number (green line in the figure) fits more closely than the curve of the -0.2 power

law. This fact indicates that the increase in loss (or the fall in performance) at lower Reynolds number can be greater than that predicted by the conventional law of the -0.2 power of Reynolds number.

Figure 24 shows the pitchwise-averaged turbulence intensity at the rotor midspan in **Figure 22**. The turbulence intensity increases dramatically with decreasing Reynolds number due to the increased wake of the rotor. The turbulence intensity at the low Reynolds number $Re_{out,RT} = 3.2 \times 10^4$ (12.3%) is 1.7 times greater than that at the high Reynolds number $Re_{out,RT} = 12.8 \times 10^4$ (7.3%).

4. CONCLUSIONS

The unsteady flow field downstream of an axial flow turbine rotor at low Reynolds numbers, $Re_{out,RT} = 3.2 \times 10^4 \sim 12.8 \times 10^4$, was investigated experimentally using hot-wire probes in a stationary frame of reference. The time-averaged and time-dependent distributions of velocity and turbulence intensity were analyzed to determine the effect of the reduction of Reynolds number.

(1) The regions of high turbulence intensity due to the wake and the secondary vortices increased dramatically with decreasing Reynolds number.
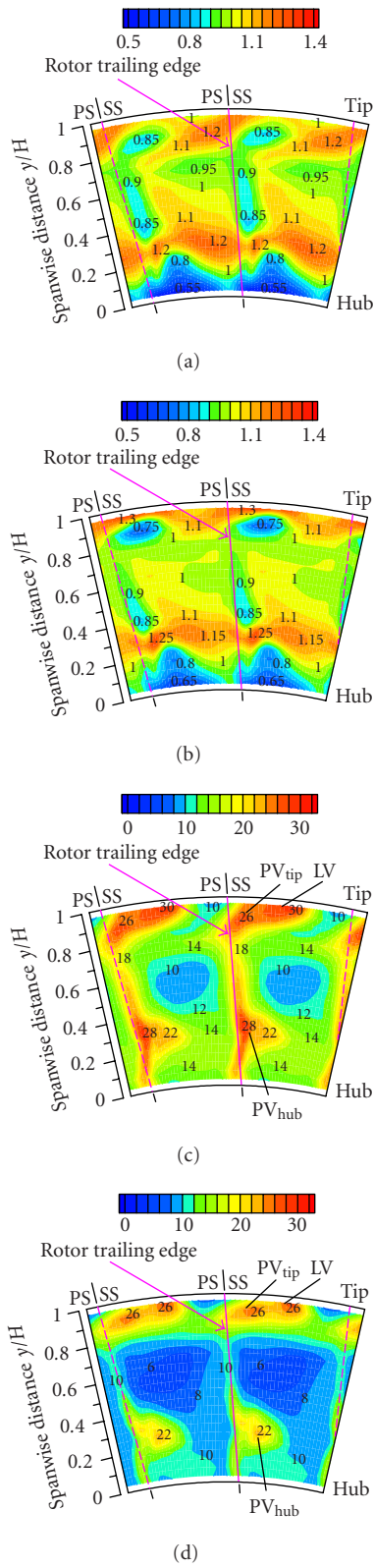
(a)

(b)

(c)

(d)

FIGURE 17: Time-averaged distributions at rotor exit in rotating frame of reference. (a) and (b) Velocity V/V_2. (c) and (d) Turbulence intensity Tu%. ((a) and (c) Lowest Reynolds number $Re_{out,RT} = 3.2 \times 10^4$. (b) and (d) Highest Reynolds number $Re_{out,RT} = 12.8 \times 10^4$).
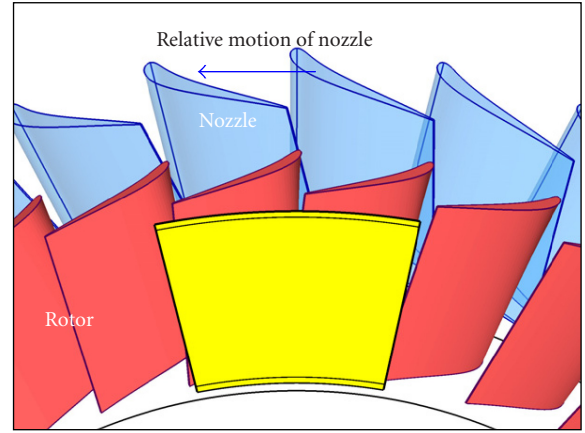

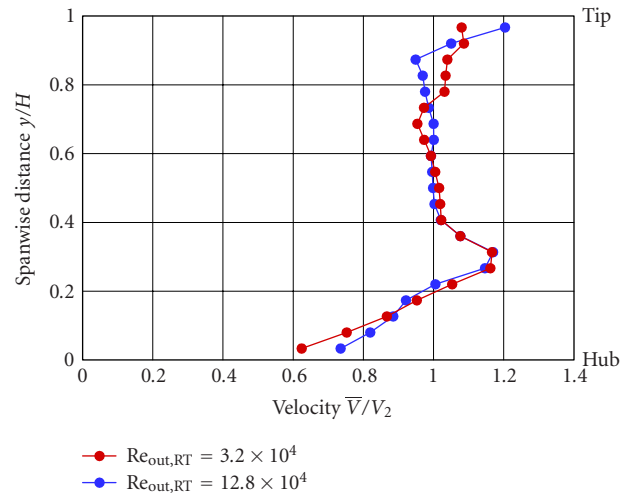FIGURE 18: Rotating frame of reference in Figure 17.

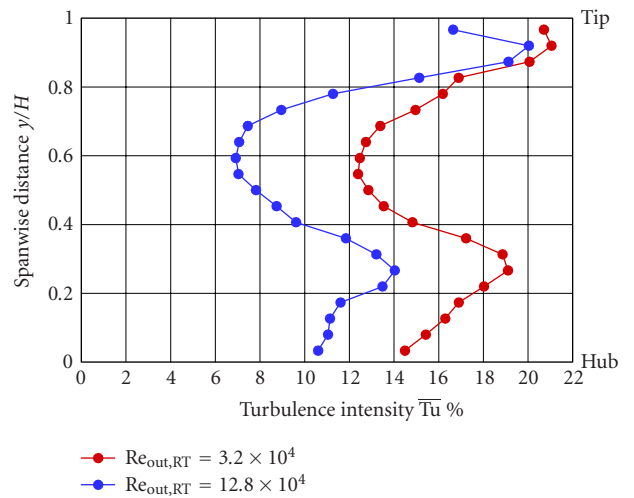FIGURE 19: Spanwise distributions of time-averaged velocity at rotor exit.

FIGURE 20: Spanwise distributions of time-averaged turbulence intensity at rotor exit.
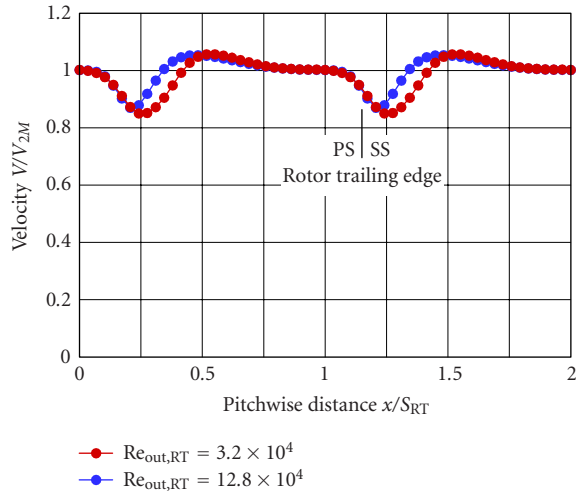
FIGURE 21: Pitchwise distributions of time-averaged velocity at rotor exit (midspan).
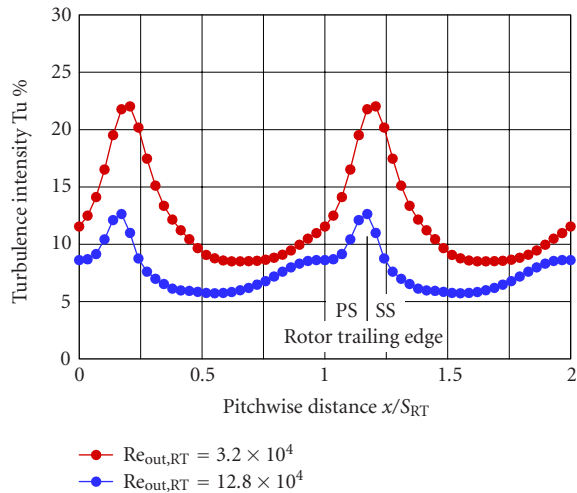

FIGURE 22: Pitchwise distributions of time-averaged turbulence intensity at rotor exit (midspan).

(2) The periodic fluctuations of the velocity and turbulence intensity due to rotor-stator interaction increased with decreasing Reynolds number. Unsteady-flow analysis is clearly important in the design of turbine blades operating at low Reynolds numbers.

(3) The energy-dissipation thickness and turbulence intensity at the rotor exit increased with decreasing Reynolds number. The time-averaged energy-dissipation thickness of the rotor midspan at the low Reynolds number $\text{Re}_{\text{out,RT}} = 3.2 \times 10^4$ was 1.5 times greater than that at the high Reynolds number $\text{Re}_{\text{out,RT}} = 12.8 \times 10^4$. Although the conventional curve of the -0.2 power of the Reynolds number agreed with the measured energy-dissipation thickness at higher Reynolds numbers, the curve of the -0.4 power law fitted more closely than the curve of the -0.2 power law at lower Reynolds numbers below 6.4×10^4.
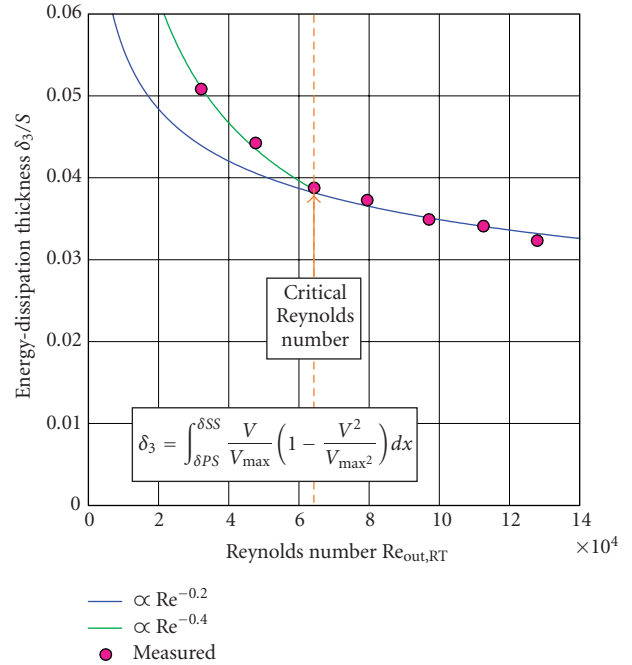

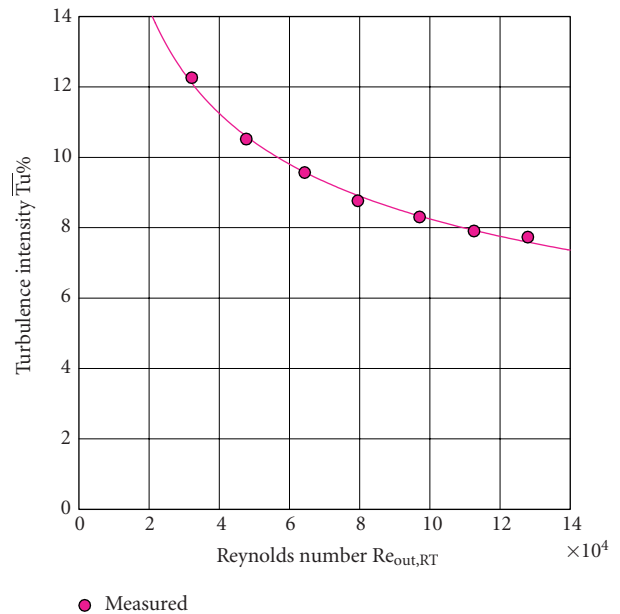FIGURE 23: Energy-dissipation thickness of rotor wake (midspan, $y/H = 0.5$).

FIGURE 24: Turbulence intensity of rotor wake (midspan, $y/H = 0.5$). (Pitchwise-averaged and time-averaged value.)

ACKNOWLEDGMENT

REFERENCES

[1] H. Arakawa, T. Suzuki, K. Saito, S. Tamura, and S. Kishi, "Research and development of 300 kW class ceramic gas turbine project in Japan," ASME paper no. 97-GT-87, 1997.

[2] E. M. Curtis, H. P. Hodson, M. R. Bangieghbal, J. D. Denton, R. J. Howell, and N. W. Harvey, "Development of blade profiles for low pressure turbine applications," *Journal of Turbomachinery*, vol. 119, no. 3, pp. 531–538, 1997.

[3] C. G. Murawski, R. S. Sondergaard, R. B. Rivir, K. Vafai, T. W. Simon, and R. J. Volino, "Experimental study of the unsteady aerodynamics in a linear cascade with low Reynolds number, low pressure turbine blades," ASME paper no. 97-GT-95, 1997.

[4] V. S. Schulte and H. P. Hodson, "Unsteady wake-induced boundary layer transition in high lift LP turbines," *Journal of Turbomachinery*, vol. 120, no. 1, pp. 28–35, 1998.

[5] R. J. Howell, O. N. Ramesh, H. P. Hodson, N. W. Harvey, and V. Schulte, "High lift and aft-loaded profiles for low-pressure turbines," *Journal of Turbomachinery*, vol. 123, no. 2, pp. 181–188, 2001.

[6] K. W. Van Treuren, T. Simon, M. von Koller, A. R. Byerley, J. W. Baughn, and R. Rivir, "Measurements in a turbine cascade flow under ultra low Reynolds number conditions," *Journal of Turbomachinery*, vol. 124, no. 1, pp. 100–106, 2002.

[7] J. P. Bons, R. Sondergaard, and R. B. Rivir, "The fluid dynamics of LPT blade separation control using pulsed jets," *ASME Journal of Turbomachinery*, vol. 124, no. 1, pp. 77–85, 2002.

[8] O. P. Sharma, T. L. Butler, H. D. Joslyn, and R. P. Dring, "Three-dimensional unsteady flow in an axial flow turbine," *Journal of Propulsion and Power*, vol. 1, no. 1, pp. 29–38, 1985.

[9] F. Kost, F. Hummel, and M. Tiedemann, "Investigation of the unsteady rotor flow field in a single HP turbine stage," ASME Paper 2000-GT-0432, 2000.

[10] H. P. Hodson, "Measurements of wake-generated unsteadiness in the rotor passages of axial flow turbines," *ASME Journal of Engineering for Gas Turbines and Power*, vol. 107, pp. 467–476, 1985.

[11] V. S. P. Chaluvadi, A. I. Kalfas, and H. P. Hodson, "Vortex transport and blade interactions in high pressure turbines," *Journal of Turbomachinery*, vol. 126, no. 3, pp. 395–405, 2004.

[12] A. Binder, W. Forster, K. Mach, and H. Rogge, "Unsteady flow interaction caused by stator secondary vortices in a turbine rotor," *ASME Journal of Turbomachinery*, vol. 109, pp. 251–257, 1987.

[13] M. A. Zaccaria and B. Lakshminarayana, "Unsteady flow field due to nozzle wake interaction with the rotor in an axial flow turbine: part I—rotor passage flow field," *Journal of Turbomachinery*, vol. 119, pp. 201–213, 1997.

[14] M. A. Zaccaria and B. Lakshminarayana, "Unsteady flow field due to nozzle wake interaction with the rotor in an axial flow turbine: part II—rotor exit flow field," *Journal of Turbomachinery*, vol. 119, pp. 214–224, 1997.

[15] T. Matsunuma and Y. Tsutsui, "LDV measurements of unsteady midspan flow in a turbine rotor at low Reynolds number," ASME paper no. GT2003-38468, 2003.

[16] A. Binder, T. Schroeder, and J. Hourmouziadis, "Turbulence measurements in a multistage low-pressure turbine," *ASME Journal of Turbomachinery*, vol. 111, pp. 153–161, 1989.

[17] H. E. Gallus, J. Zeschky, and C. Hah, "Endwall and unsteady flow phenomena in an axial turbine stage," *Journal of Turbomachinery*, vol. 117, pp. 562–570, 1995.

[18] D. E. Halstead, D. C. Wisler, T. H. Okiishi, G. J. Walker, H. P. Hodson, and H. Shin, "Boundary layer development in axial compressors and turbines part 4: computations & analyses," ASME paper no. 95-GT-464, 1995.

[19] L. Fielding, *Turbine Design: The Effect on Axial Flow Turbine Performance of Parameter Variation*, ASME Press, New York, NY, USA, 2000.